Carbonized Polymer Dots-based Spectrally Adaptable Photonic Microbarcodes

Barun Kumar Barman[1*], Keisuke Watanabe[1], Tadaaki Nagao [1, 2*]

Dr. B. K. Barman, Dr. K. Watanabe, Dr. T. Nagao

Research Center for Materials Nanoarchitectonics (MANA), National Institute for Materials Science (NIMS), Tsukuba, Ibaraki 305-0044, Japan

Dr. T. Nagao

Department of Condensed Matter Physics, Graduate School of Science, Hokkaido University, Sapporo, Hokkaido 060-0810, Japan

E-mail: BARMAN.Kumarbarun@nims.go.jp, NAGAO.Tadaaki@nims.go.jp

Keywords: Carbonized polymer dots, multicolor emission, microemitter, whispering gallery mode, photonic barcode, anti-counterfeit

Carbonized polymer dots (CPDs) are versatile nanomaterials with remarkable optical properties that enable their use in a wide range of photonics applications. CPDs exhibit excitation-wavelength-dependent tunable emissions that span the visible to near-infrared (NIR) spectrum. In this study, whispering-gallery-mode (WGM) emission achieved using CPDs-coated monodisperse polystyrene (CPDs@PS) microbeads is used to develop wavelength-adaptable photonic barcodes by leveraging the excitation-dependent photoluminescence of CPDs. Each resonant emission peak acts as a unique fingerprint of photonics barcodes related to the corresponding microresonator caused by WGM emission. These photonic barcodes can be easily disguised and then decoded by varying the excitation wavelength. WGM-based barcodes can exhibit a large number of encoding capacities by adjusting the resonator diameter. Monodisperse CPDs@PS microbeads (3, 4.5, and 6 μm) are used to demonstrate adaptable photonic barcodes, which can improve the readability and reproducibility of spectral patterns for the reliable tagging and identification of commodities. Unlike traditional semiconductor quantum dots or dye-doped microresonators, this adaptive resonant emission does not require structural or chemical modifications, making it an ideal candidate for multiplexed assays, cell tagging and tracking, anti-counterfeiting, and for ensuring the integrity and authenticity of products in various high-value sectors.

1. Introduction

Counterfeiting poses a major threat to various industries, including those dealing with high-value products, such as pharmaceuticals, electronics, luxury goods, and currencies. [1] The global economic impact of counterfeit goods is staggering, with annual losses amounting to hundreds of billions of dollars.[2] Besides financial losses, counterfeit products also compromise safety, erode brand trust, and undermine regulatory frameworks;[3] therefore, developing advanced anti-counterfeiting technologies is critical for ensuring product integrity, consumer safety, and brand protection. To this end, one promising approach is utilizing advanced microresonator-based photonic materials, which can promote the development of spectrally encrypted codes and tags.[4] Thus far, different types of microcavities and microlasers have been employed for spectroscopic coding applications.[5] Among these, whispering-gallery-mode (WGM) microcavities, which are shaped as microspheres or microdisks, are most frequently utilized for spectral barcoding.[6] A WGM-based microcavity is a micro-object with a circular cross-section, such as a microsphere, microdisk, or microring.[7] These micro-objects require smooth surfaces and a higher refractive index than their surrounding material to confine light. Light is guided along the perimeter via total internal reflection at the microcavity surface, resulting in either transverse electric (TE) or transverse magnetic (TM) modes.[8] Small variations in the microcavity size, even below the diffraction limit, can cause detectable spectral shifts. In microspheres, fluorescent dyes,[9] semiconductor quantum dots,[10] semiconductors,[11] carbonized polymer microspheres,[12] upconverting nanoparticles,[13] or dye-doped solid spheres fabricated from organic or semiconducting materials are typically used as the gain material, [14] and these non-deformable beads are often used for barcoding.[15] In microcavity barcodes, information is encoded through the properties of the emitted light based on the size, shape, and gain material of the microcavity.[16] These microcavity barcodes can be randomly sized because of the inherent variability in microcavity properties, or they can be predefined for encoding specific information.[17] Most experimentally demonstrated random-sized microcavity-based barcodes lack predefined information and rely on the natural randomness of manufacturing, such as size polydispersity. This randomness is advantageous for creating complex and difficult-to-replicate barcodes with useful applications in anti-counterfeiting and tagging numerous entities.[6b, 12, 18] Encoding specific information in macroscopic barcodes requires precise manufacturing control, and some cases of predefined microcavity barcodes have been demonstrated.

Carbon dots (CDs) have emerged as ideal candidates for bioimaging, sensing, and optoelectronics applications because they are rare-earth and metal-free nanomaterials that offer high photoluminescence (PL), tunable emission, and excellent stability.[19] Carbonized polymer dots (CPDs) are a type of carbon dots characterized by a hybrid structure that incorporates both polymeric and carbon-based complex structures. CPDs are typically synthesized via dehydration, polymerization, and carbonization during the solvothermal process. These CPDs are rich in nitrogen and oxygen and have a large number of surface functional groups. Furthermore, CPDs have gained attention for use in anti-counterfeiting applications because of their ability to emit light of multiple colors in the visible to near-infrared (NIR) wavelengths, which serve as dynamic optical markers and secret inks. [20] Despite the potential of CPDs in anti-counterfeiting, their application in generating solid-state fluorescence (SSF) materials for realizing spectrally adaptable photonic barcodes is yet to be explored.

This study demonstrates the use of CPDs in the development of advanced SSF materials that can function as fluorescent photonic barcodes. We investigate the integration of CPDs into predefined spherical microresonators to harness their photonic properties across the visible to NIR spectrum. Distinct spectroscopic codes generated by WGM emission are closely linked to the diameter of the microbeads; however, random variation in microbead diameters hinders the replication of their spectral barcodes, making tagging unreliable. We employed monodisperse polystyrene (PS) microbeads with predefined diameters (3, 4.5, and 6 μm) and low coefficient of variation (CV < 3%) to ensure accurate and readable photonic barcodes for tagging commodities. This approach improves the consistency and readability of the spectral patterns, leading to more reliable tagging and identification. The use of CPDs in microresonators presents several advantages over traditional semiconductor quantum dots or dye-doped microresonators: (1) CPDs provide excitation-dependent emission without the need for structural or chemical modifications, offering a more powerful and versatile approach for creating photonic barcodes with high security. (2) The intrinsic properties of CPDs, such as their high stability and tunable emission, render them ideal candidates for long-lasting and reliable anti-counterfeiting tags. The development of CPDs-based SSF materials with adaptive photonic barcodes represents a major advancement in the security features, offering a robust and scalable solution to combat counterfeiting and protect valuable products.

2. Results and Discussion

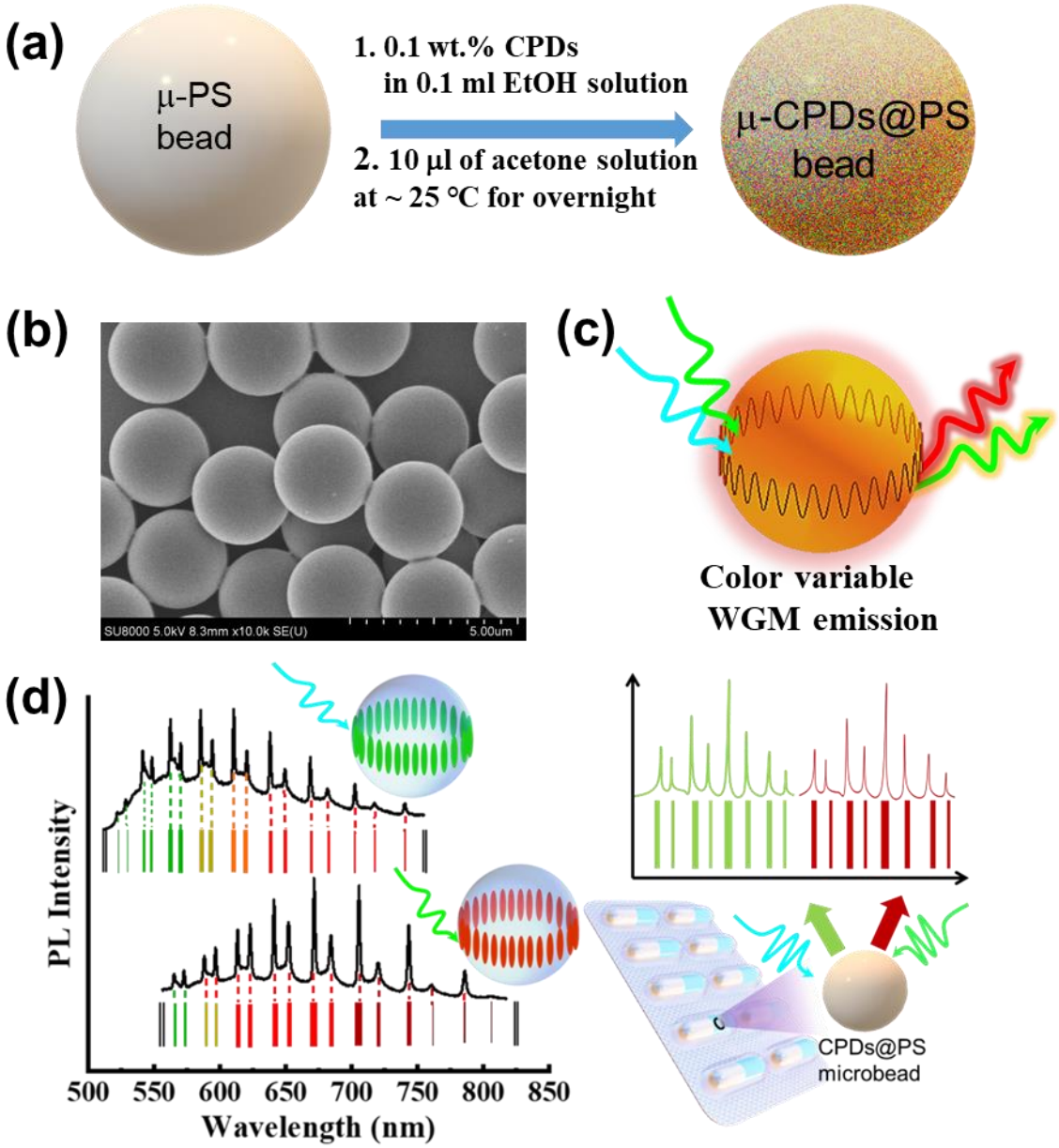

Figure 1. (a) Protocol for surface coating micro-polystyrene (μ-PS) beads with carbon dots (CPDs). (b) Scanning electron microscopy image of 3 μm of PS beads. (c) Schematic of the spectrally tunable whispering-gallery-mode (WGM) emission from the microresonator by simply varying the excitation light source. (d) WGM emission from the 3μ-CPDs@Ps beads via changing the excitation source from 470 nm to 532 nm, and schematic representation of corresponding color adaptable photonic barcodes for anticounterfeit tagging applications.

Multicolor emissive CPDs were synthesized using citric acid (CA) and urea in a formamide solution via the solvothermal method and exhibited excitation wavelength-

dependent emission spectra. The high temperature and pressure during the solvothermal reaction promoted efficient condensation, polymerization, and carbonization through reactions between CA and urea. These conditions facilitate the incorporation of heteroatoms such as nitrogen and oxygen into the carbon framework. Additionally, the presence of specific functional groups in the precursors and cross-linked polymerization structures enhances the abundant surface functionalization of CPDs, including amines, carboxylic acids, hydroxyls, and amides. The surface-coating process involved incorporating CPDs into commercially available polystyrene (PS) microbeads of various diameters (3, 4.5, and 6 μm) by infusing them in an ethanol-acetone mixture (**Figure 1**a). Acetone causes swelling of the near-surface region of PS and generates nanopores, into which CPDs can diffuse together with the solution and trapped at the surface of the PS microbeads. The high number of surface functional groups of the CPDs facilitates their adsorption onto the PS surface and may promote diffusion from the solution phase and coat the microbeads uniformly. After coating, the microspheres are separated from excess CPDs and dried, yielding coated PS beads for further applications. The scanning electron microscope (SEM) image shows examples of monodispersed PS beads with a diameter of 3 μm (**Figure 1**b). The image highlights the uniform size and smooth surface of PS beads, which are crucial for achieving consistent WGM emission performance. This schematic illustrates the principle of spectrally adaptable WGM emission from a microreactor by varying the excitation light source (**Figure 1**c). This tuning capability is essential for applications that require precise control for predefined readable coding. For example a barcode comprises a series of black bars of varying widths, with each bar representing a different digit.[21] In contrast, WGM emission-based barcodes are defined differently; each solid bar corresponds to the wavelength position of a resonant mode in the PL spectrum (black line in **Figure 1**d). The width of each bar is determined from the relative fluorescence intensity at the same wavelength as that in the TM or TE resonance mode. **Figure 1**d shows the generation of spectrally reconfigurable WGM emission-assisted photonics barcode from an identical 3 μm CPDs-coated monodisperse polystyrene (CPDs@PS) beads when the excitation source is changed from 470 to 532 nm. The WGM-emission-assisted spectral characteristics vary with the excitation wavelength (spectrally tunable greenish and red barcodes at 470 and 532 nm excitation, respectively), wich indicates the capability of applying this phenomenon to the doubly protected barcoding. The corresponding microphotoluminescence (μ-PL) image of a microsphere with predefined size confirms the successful integration of photonic resonance and CPDs' luminescent functionalities within the PS beads. The ability to vary the excitation source and changing the

resulting WGM emission spectra is critical for spectrally reconfiguring and doubly predefined barcode tagging applications.

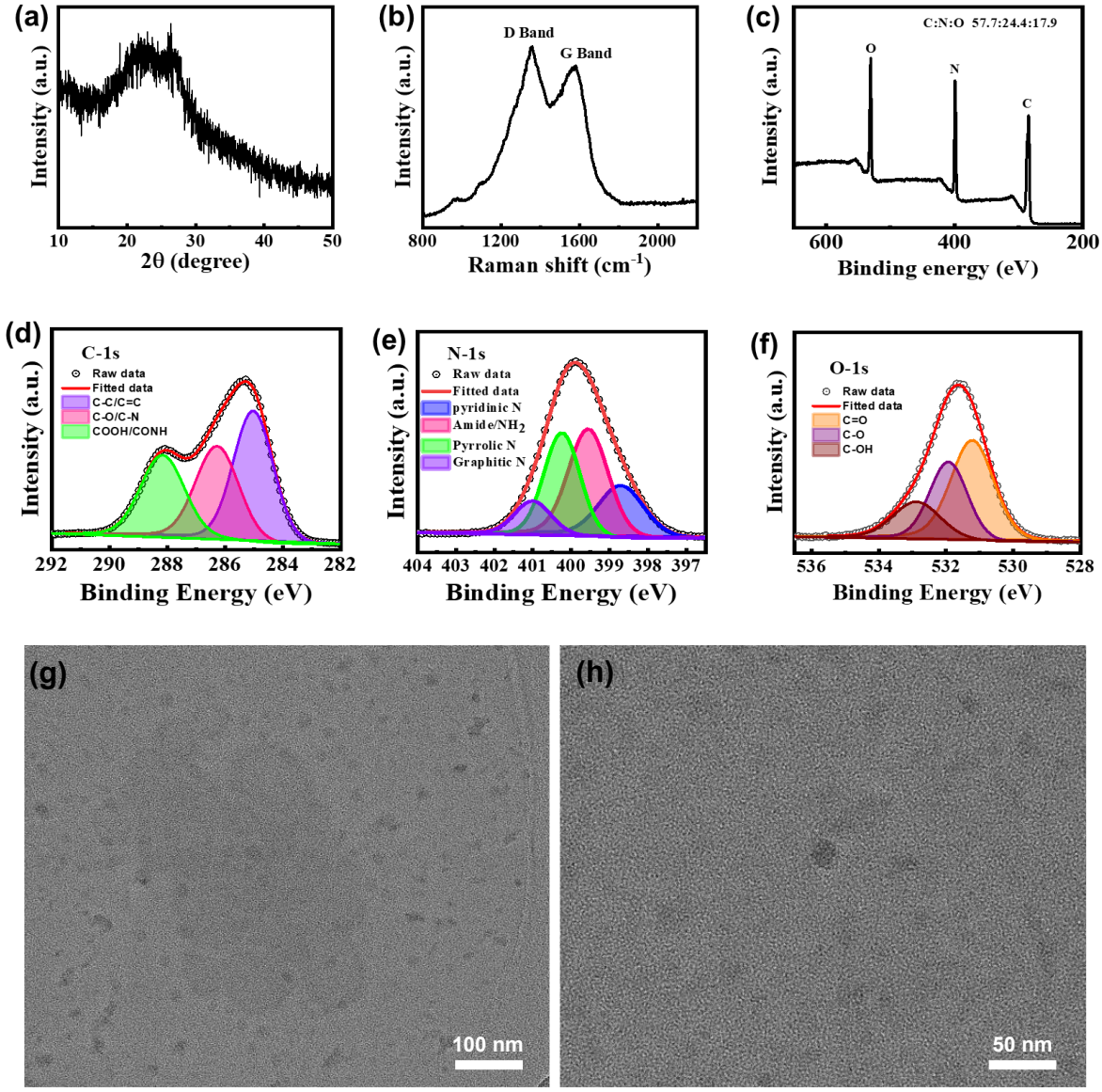

Figure 2. (a and b) XRD pattern and Raman spectra of CPDs X-ray photoelectron spectroscopy (XPS) survey spectra. (c) XPS survey spectra. (d –f) Deconvoluted high-resolution XPS spectra of C-1s, N-1s, and O-1s of CPDs. (g and h) low and high magnified TEM images of CPDs.

The structural and chemical characteristics of the CPDs were investigated using various techniques. The X-ray diffraction (XRD) patterns (**Figure 2**a) reveal a broad peak intensity at a 2θ value of 21–26°, indicating small particle sizes and a d value of 0.336 nm, which corresponds to amorphous structures and the (002) plane of graphitic lattice structures.[22] Raman spectroscopy (**Figure 2**b) shows D and G band peaks at 1360 and 1580 cm^{-1},

respectively, with an I_D/I_G ratio of ~0.94, suggesting a high number of defects and disordered (sp^3) structures within the graphitic (sp^2) framework.[23]

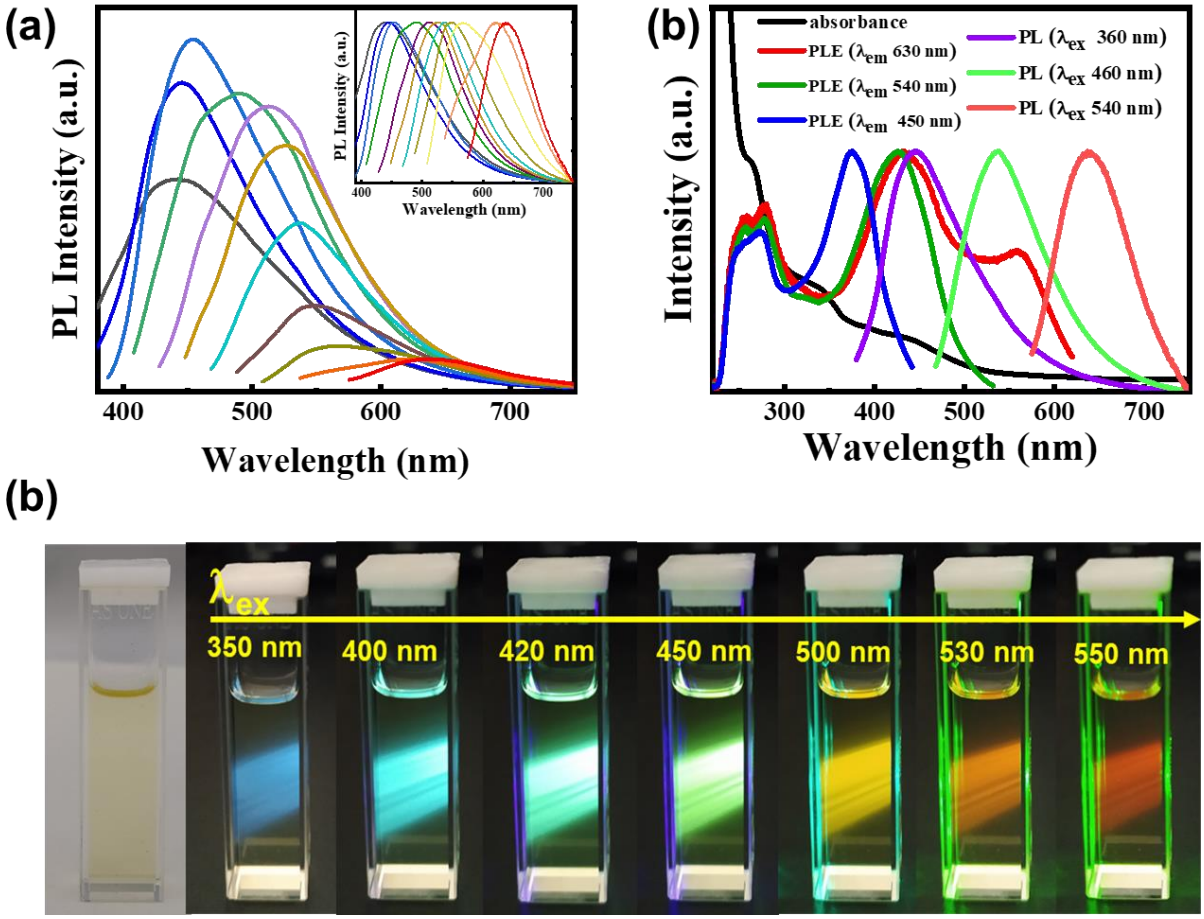

Figure 3. (a) Emission spectra of the CPDs in EtOH solution excited at 340−540 nm in 20 nm increments. The inset shows corresponding normalized emission spectra. (b) UV-visible and PL and corresponding excitation spectra of colloidal CPD solution. (c) Digital photographs of the colloidal CPDs solution captured under daylight (left) and under different excitation wavelengths from 350 to 550 nm.

The X-ray photoelectron spectroscopy (XPS) analysis (**Figure 2**c) confirms the presence of C, O, and N with atomic percentages of 57.7, 24.4, and 17.9%, respectively. High-resolution XPS (HRXPS) spectra for C 1s (**Figure 2**d) indicate various chemical bonds, including C-C/C=C, C-O/C-N, and COOH/CONH, which point to the presence of diverse functional groups.[24] HRXPS spectra for N 1s (**Figure 2**e) show four peaks at binding energies of 398.4, 399.3, 400, and 401.2 eV, which correspond to pyridinic, pyrrolic, amide, and graphitic N-doping sites, respectively, with amide and pyrrolic peaks being the most prominent during CD formation.[25]

Deconvoluted O 1s spectra (**Figure 2**f) further confirm three types of C-O bonds in CPDs. Attenuated total reflectance Fourier transform infrared (ATR-FTIR) spectroscopy shows peaks corresponding to the hydroxyl, amide, carbonyl, acid, and amine groups (**Figure S1**).[24, 25b] Overall, these analyses demonstrate the presence of various functional groups and N-doping sites in CPDs, influencing their absorption and emission properties. The TEM images of CPDs display nearly spherical particles (**Figures 2**g and h) with sizes ranging from ~7–10 nm. Although the resolution of these images is not very high, they do not show recognizable lattice fringes, suggesting that the carbogenic core is nearly amorphous and has a high level of surface functionalization.[26] Figure 3a shows the emission spectra of colloidal CPDs in ethanol at various excitation wavelengths. The spectra display the relative intensities, whereas the inset shows the corresponding spectra on a normalized scale. The results reveal a clear dependence of the emission on the excitation wavelength. As the excitation wavelength increases, the fluorescence band maximum shifts to longer wavelengths, accompanied by a gradual narrowing of the emission bandwidth and a decrease in the emission intensity. Figure 3a and the 3D excitation fluorescence spectra of CPDs under various excitation wavelengths, ranging from 340–560 nm, demonstrate the full-color emission capability in the entire visible spectra of CPDs produced via a solvothermal reaction in formamide (**Figure S2**). **Figure 3**b illustrates the UV-Vis absorption spectra of the CD solution, indicating a strong absorption at 200 nm and a broad peak at 340 nm, corresponding to π-π* and n-π* transitions of C=C bonds C=O and C-N bonds corresponding to the surface states and conjugated π structures. Broad absorption bands at lower energies (approximately 450 nm and 550 nm) are typical for CPDs emitting in the red range, which indicates a narrowed electronic band gap.[24b, 27] The direct and indirect electronic transitions of carbonized polymer dots (CPDs) are evaluated to be 3.2 eV and 1.81 eV, respectively, as determined using the Tauc equation (**Figure S**3). The band gap energies of the direct transitions are higher than those of the indirect transitions for CPDs. Photoluminescence excitation (PLE) spectra provide insight into electronic absorption characteristics. The PLE spectra corresponding to blue, green, and red emissions reveal distinct wavelength-dependent electronic excitations of the CPDs, correlated with the multiple peaks in the absorption spectra (Figure 3b). Functional groups, such as -COOH and graphitic N centers in CPDs, create states (O and N) that cause green and red emissions.[25b, 28] These groups and doping centers introduce mid-gap states into the HOMO-LUMO gap of CPDs, resulting in red-shifted absorption and low-energy fluorescence in the visible spectrum. These transitions arising from sub-bandgap states contribute to the emissions of CPDs, which vary with the excitation intensity. Figure 3c shows photographs of the colloidal CPDs solutions demonstrating their full-color emission

across the entire visible wavelength. Both the emission spectrum and accompanying digital photographs clearly reveal the excitation-dependent fluorescence exhibited by the CPDs (**Figures 3b** and **3c**).

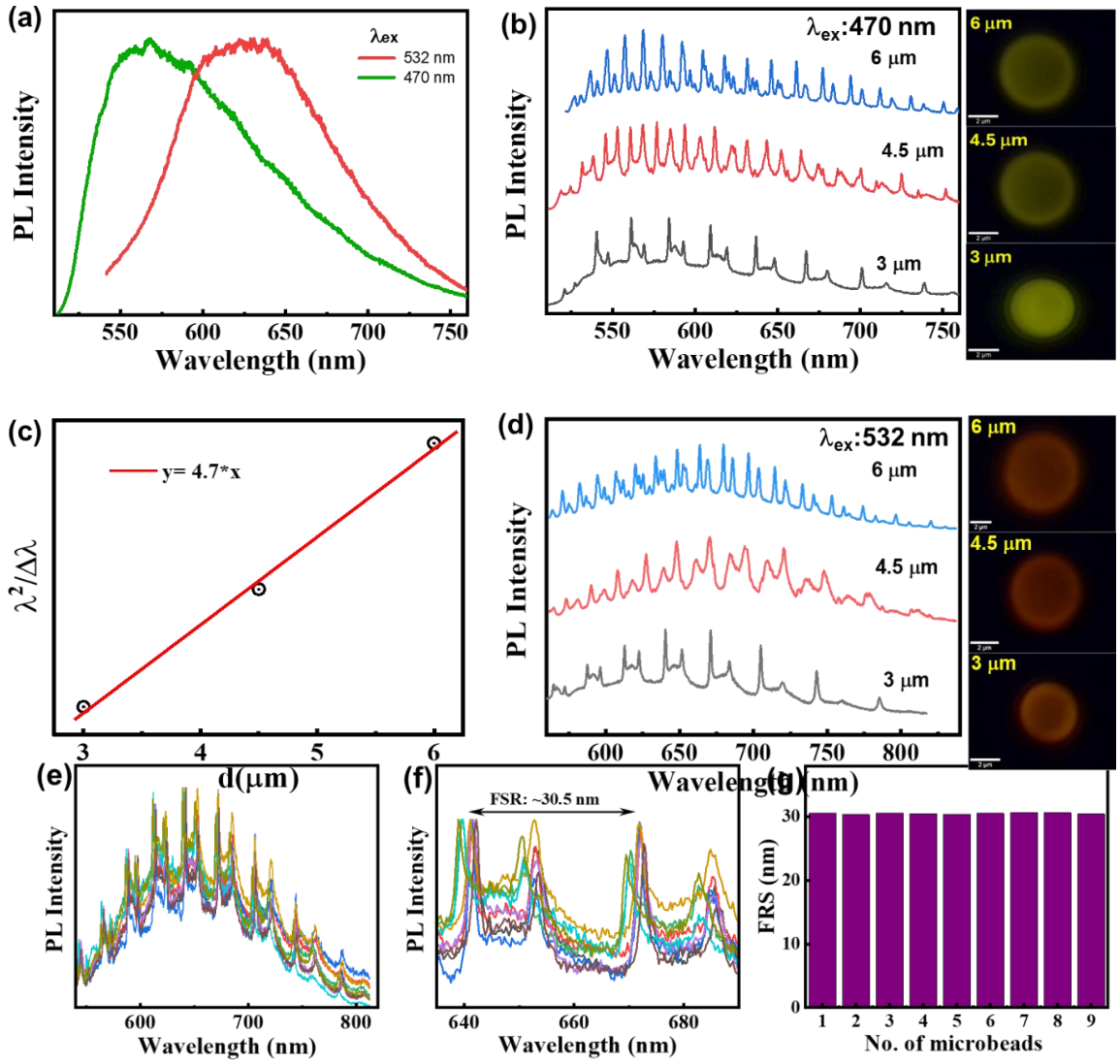

Figure 4. (a) μ-PL spectra of the CPDs@PVP film at 470 and 532 nm excitation. (b) WGM mode emission of CPDs@PS in three microbeads with different diameters and their corresponding μ-PL images under 470 nm excitation. (c) Relationship between $\lambda^2/\Delta\lambda$ and the diameter of microbeads. The red line represents a linear fit to the function $\lambda^2/\Delta\lambda = n\pi d$. (d) The WGM mode emission of CPDs@PS microbeads in three different diameter microbeads and their corresponding μ-PL images under a 532 nm excitation. (e) WGM emission from multiple 3 μm-CPDs@PS microbeads under a 532 nm excitation. (f) Magnified μ-PL spectra and FSR. (g) Comparison of FSR values from multiple microbeads at the red wavelength range.

Figure 4a shows the μ-PL spectrum of the CPDs@PVP film under 470 and 532 nm laser excitation, revealing greenish-yellow and red emissions corresponding to the excitation wavelength-dependent properties of CPDs in solid-state. Adaptable multilevel photonic barcoding applications have been successfully demonstrated by leveraging the emission color variations with changing excitation wavelengths. Monodisperse CPDs@PS microbeads with predefined diameters (3, 4.5, and 6 μm) have been utilized for generating precise and easily readable photonic codes applicable for commodity tagging (**Figure S4**). A μ-PL system utilized 470 and 532 nm lasers as pump sources to explore the cavity effect of CPDs@PS microbeads. Sharp peaks superimposed on a broad emission spectrum were observed at the edges of the microbeads with three different diameters (**Figure 4**b) under 470 nm laser excitation. These spectra exhibit two distinct peaks arising from the breakdown of degeneracy in the TE and TM modes within the WGM resonator (**Figure 4b**). In addition, the μ-PL image reveals a prominent green ring-shaped pattern at the microbead perimeters (**Figure 4b**, right), which can be attributed to the WGM resonant cavity effect. The WGM resonator operates according to the equation $m\lambda = n_{eff}\pi d$, where m, λ, n_{eff}, and d represent an integer, resonant wavelength, effective refractive index of the mode, and diameter of the microbead, respectively.[6e, 17d, 29] The resonant wavelength λ in a WGM resonator depends on the size and refractive index of the microbeads. Each microbead exhibits unique spectral patterns, which serve as its specific fingerprint, and they are used as an optical barcode. The mode spacing (Δλ) of the WGM emission, also known as the free spectral range (FSR), decreases significantly from 21, 15, and 11 nm at ~550 nm as the diameter increases from 3 to 4.5 to 6 μm, respectively (**Figure S5**). According to the WGM theory, the mode spacing Δλ and diameter d are related by $\lambda^2/\Delta\lambda = n_{eff}\pi d$, where λ represents the wavelength of the guided light, and n_{eff} represents the effective refractive index.[30] **Figure 4c** illustrates the relationship between $\lambda^2/\Delta\lambda$ and d. The linear fitting of the data shows a slope of 4.9 for $n_{eff}\pi$. Given that π is a constant (~3.14), n_{eff} is calculated to be 1.49, which is closer to the refractive index of bare PS (**Figure 4c**). This implies that the surface functionalized CPDs layer on the PS microbead does not alter the refractive index of PS. The microresonator exhibits red-NIR wavelength range WGM emission when excited by a 532 nm light source; this is observed in the 3, 4.5, and 6 μm microresonators, as shown in the corresponding μ-PL spectra and images (**Figure 4d**). The FSR in the red wavelength region gradually decreases from 31 nm to 22 nm and to 16 nm as the microresonator diameter increases from 3 μm to 4.5 μm and 6 μm, respectively (**Figure S6**). The relationship between the WGM resonance and the diameter of the microbeads plays a key role in generating distinct spectroscopic barcodes. The uniformity

of monodisperse PS microbeads, with predefined diameters and a low coefficient of variation (CV < 3%), results in nearly identical WGM emissions from multiple microbeads, as shown in **Figure 4e** for the 3-μm CPDs@PS microbeads under a 532 nm excitation. Identical WGM emission can be achieved from multiple 3 μm CPDs@PS microbeads using a 470 nm excitation (**Figure S7**). The FSR of multiple microbeads is nearly identical (~ 30.5 nm) in the red wavelength region (**Figures 4f** and **g**). Similarly, the WGM emission and FSR observed for multiple 6 μm CPDs@PS microbeads display nearly identical characteristics, indicating a consistent response across the sample set (**Figure S8**). This method enhances the readability and reproducibility of the spectral patterns, enabling more reliable tagging and identification.

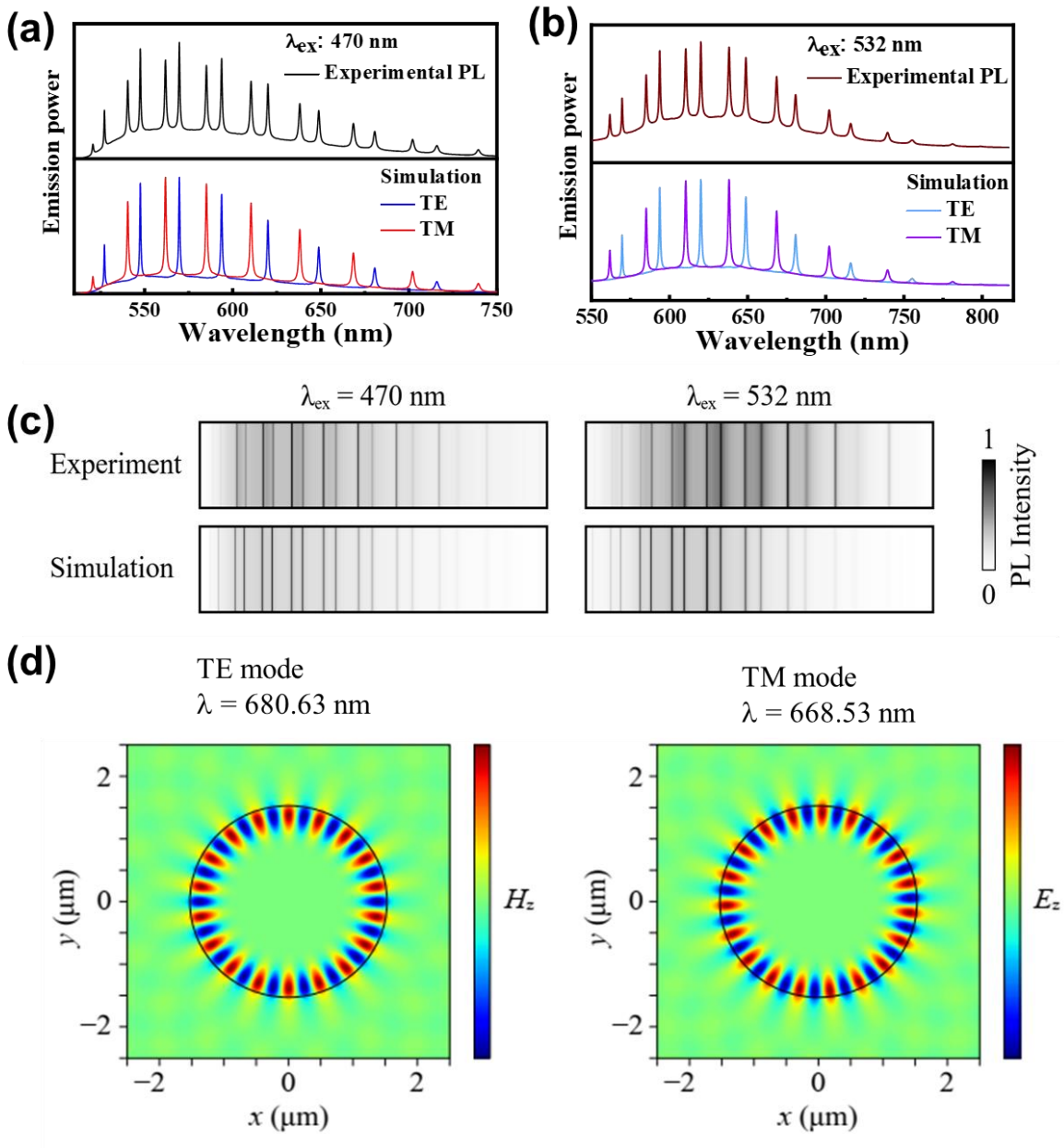

Figure 5. (a and b) Experimental and simulated PL spectra of a 3-μm CPDs@PS resonator excited at 470 and 532 nm. (c) Comparison of wavelength-adaptable photonic barcodes for experiment (upper) and simulation (lower). (d) Electromagnetic field distributions of TE (left) and TM (right) resonances in the red wavelength region.

The experimental PL spectra across the two distinct spectral regions, along with the field profiles, were simulated using the finite-difference time-domain (FDTD) method. The simulated WGM resonances in the greenish-yellow and red wavelength regions, combined with background emissions from the 3-μm CPDs@PS microbeads, closely aligned with the experimental spectra obtained under 470 nm and 532 nm laser excitation (**Figures 5**a and 5b).

These emission spectra indicate contributions from both TE and TM modes within the microbeads. The differences in the optical paths naturally lead to variations in the mode separation for each WGM type, resulting in non-uniform spectral separation of the resonant peaks. We selected microbeads with specific diameters to examine the readouts for tagging purpose. Figure 5c presents both the simulated and experimental WGM emission patterns, demonstrating the construction of photonic barcodes in the greenish-yellow and red-NIR wavelength ranges by altering the excitation wavelength from 470 nm to 532 nm. In addition, Figure 5d shows mode profiles at WGM resonance peaks near 680 and 666 nm, with the Hz profile for the TE mode and the Ez profile for the TM mode, respectively, highlighting the characteristics of the fundamental TE and TM modes with a radial mode number of 1. In addition, based on an automated numerical simulation, the CD-coated layer radius and refractive index (n_{CD}) were evaluated (detailed in the Experimental Section). Based on the optimized spectra, the CPDs layer thickness is ~ 29 nm, and the n_{CD} is ~1.55, which is consistent with previously reported values.[31]

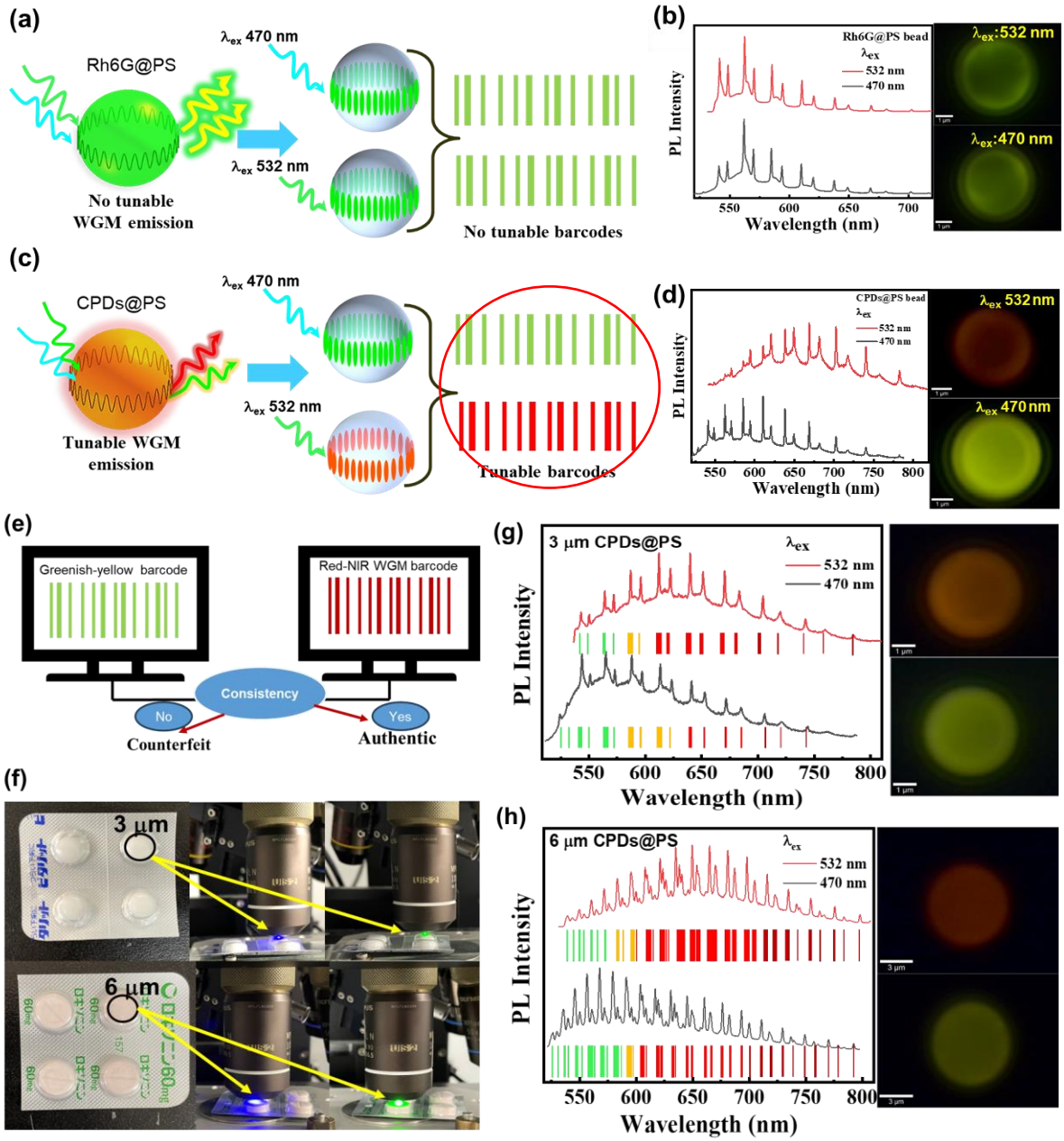

Figure 6. (a and b) Schematic of the WGM emission-based photonics barcodes from 3 μm Rh6G@PS micro-resonator by varying the excitation wavelength by 470 and 532 nm and their corresponding μ-PL spectra and image. (c and d) Schematic of the spectrally tunable WGM emission from greenish-yellow to red-NIR wavelength by altering the excitation wavelength by 470 and 532 nm and their corresponding μ-PL spectra and image. (e) Color adaptable two barcodes from the same microresonator for the doubly protected authentication/tagging strategy. (f) Proof-of-concept demonstration of a color-adaptable CPDs@PS-based photonic barcode tagging on two different medicine packs by varying the excitation wavelength for drug identification (and also anti-counterfeiting). (g and h) WGM-based spectrally tunable barcodes tagging from 3 μm and 6 μm CPDs@PS microbeads on the marked region from two different drug packages.

Spectrally adaptable barcodes based on CPDs offer stronger authentication than traditional dye-doped microresonators owing to their wavelength-dependent excitation properties. **Figure 6**a illustrates the non-tunable WGM emission of dye-doped microresonators, which can only generate a single barcode by varying the excitation wavelength. For example, Rhodamine 6G-coated 3-µm polystyrene microbeads (3-µm Rh6G@PS) can produce similar spectral patterns when the excitation wavelength is changed, posing a remaining risk of counterfeiting (**Figure 6**b). A single CPDs@PS microresonator can produce spectrally tunable barcodes by simply adjusting the excitation wavelength, as depicted in **Figure 6**c. **Figure 6**d shows the spectrally tunable WGM emission and the corresponding µ-PL image obtained by changing the excitation wavelength, which generates two distinct barcodes. **Figure 6**e shows a schematic of the application of secure barcodes for authentication. Two different barcodes can be generated by simply altering the excitation source, thereby enabling product authentication with higher accuracy. If a microbead-based generated barcode is tunable, it can confirm the authenticity of a product; otherwise, the product is counterfeit. As a proof-of-concept, 3 and 6 µm CPDs@PS microbeads were applied as "security tags" on two different drug packages. The µ-PL spectrum and images were recorded by varying the excitation wavelength from blue to green (**Figure 6**f). Drug packages 1 and 2 are tagged with 3 µm and 6 µm CPDs@PS microbeads for authentication purposes. The 3 µm CPDs@PS microbeads demonstrated color-adaptable photonic barcodes, as evidenced by the WGM emission shown in **Figure 6**g. The corresponding µ-PL image shows greenish-yellow and red emissions from the microbeads. Similarly, **Figure 6**h shows the wavelength-tunable WGM emission and generated two different barcodes and associated µ-PL images, which range from greenish-yellow to red from a 6 µm CPDs@PS microresonator. These readable photonic barcodes can be easily disguised and decoded on the corresponding tagged drug package by simply changing the excitation wavelength. The barcoding capacity can be enhanced by increasing the number of sharp lines in WGM-based emission spectra. This can be achieved by increasing the diameter of the resonator, which indicates a larger light confinement volume. This reduces the FSR (free spectral range; the separation between the peaks of the TM and TE modes), allowing more peaks to be observed within a given spectral range. Because the CPDs are uniformly coated on the surface of the PS and diffused deep into the subsurface region, ethanol washing of the microresonator does not significantly affect the WGM emission. (**Figure S9**). These microbeads are stable under atmospheric conditions and exhibit WGM emission even after 6 months of storage under ambient conditions (**Figure S10**). These wavelength-tunable barcodes generated from the CPDs@PS microresonator offer

enhanced security with potential applications in other systems, such as identity documents, electronics, and banknotes. In this study, the tunable excitation wavelength and simplified reading process of the covert photonic barcodes contribute to improved security features.

3. Conclusion

This study highlighted the successful integration of CPDs into spherical microresonators for the development of advanced SSF materials that can function as fluorescent spectral barcodes. We addressed the challenges associated with the readability of spectral barcodes by using monodisperse PS microbeads with predefined diameters. This approach ensures more consistent and reliable photonic barcodes, significantly enhancing the accuracy and readability required for effective tagging and identification. The inherent advantages of CPDs, including their excitation-dependent emission, high stability, and variable emission properties, render them superior to traditional semiconductor quantum dots or dye-doped microresonators for anti-counterfeiting applications. The development of CPDs-based SSF materials not only represents a breakthrough in security features but also provides a scalable and robust solution to combat counterfeiting, protecting valuable products in the marketplace. Integrating CPDs into spherical microresonators paves the way for next-generation anti-counterfeiting technologies that combine nanophotonics and materials chemistry to develop advanced SSF materials with adaptive photonic barcodes with multilevel encoding.

4. Experimental Section

Synthesis of CPDs: Citric acid monohydrate (CA, 25 mg/mL), urea (25 mg/mL), and formamide solution (20 mL) were mixed for 10 min by sonication. The solution was then transferred to a 50 mL Teflon container and placed in an autoclave crucible for a solvothermal reaction. The solution was heated at 180 °C for 6 h to synthesize CPDs and cooled to room temperature after the reaction. A dark reddish-brown solution was obtained from the initial transparent solution. The dark solution was centrifuged at 8000 rpm for 5 min and passed through a 0.2-μm syringe filter to remove larger particles. Unreacted or fragmented CA and small molecular impurities were removed by dialysis using DI water and an osmosis membrane (molecular weight cut-off = 3.5 kDa) for 24 h. Then, the solution was passed through a 20 nm filter to collect the final colloidal CPDs. The collected CPDs were dispersed in EtOH, mixed with a polyvinylpyrrolidone (PVP) matrix, and dried at 60 °C for further characterization and PL measurements.

Surface Coating of CPDs and Rh6G onto PS Microbeads: CPDs were first dispersed in an ethanol solution. A 0.1 wt.% CPDs solution was then injected into the PS microbeads with diameters of 3, 4.5, and 6 μm, which were commercially sourced from Polyscience, Inc. Acetone (10 μl) was added to facilitate the incubation of the CPDs on the surface of the PS microbeads, and the mixture was allowed to incubate overnight. After incubation, the CPDs@PS microbeads were dispersed in ethanol and drop-cast onto a glass substrate for measurement. Similarly, a 0.1 mM Rh6G ethanolic solution was incubated with 3 μm PS microbeads to achieve dye functionalization. For drug tagging applications, 3 and 6 μm CPDs@PS microbeads were dispersed in an aqueous solution, drop-cast onto the two different drug packages, and dried at room temperature.

Characterization: The CPDs were analyzed using X-ray diffraction (XRD) with a RINT-Ultima III system from Rigaku Corporation, utilizing Cu Kα radiation (λ = 1.5406 Å). The composition and chemical bonding states of the CPDs were examined via X-ray photoelectron spectroscopy (XPS) with a PHI Quantera SXM instrument (ULVAC-PHI, Inc.), using Al Kα as the X-ray source. The chemical structure was further investigated using attenuated total reflectance Fourier-transform infrared (ATR-FTIR) spectroscopy, employing a Nicolet iS50 FTIR instrument (Thermo Fisher Scientific Inc.). The absorbance spectra of the colloidal dispersions were obtained using a V-570 UV-Vis-NIR spectrometer (JASCO Corp.), whereas the fluorescence spectra were measured using an FP-8650 NIR Spectrofluorometer (JASCO Corporation).

μ-PL Measurements: The study of WGM emission and μ-Pl imaging was conducted using a WITec μ-PL system (WITec alpha300 confocal microscope) equipped with a Princeton Instruments Acton SP2300 monochromator (300 grooves/mm grating) and an Andor iDus DU-401A BR-DD-352 CCD camera. A 100x objective lens (NA = 0.9, MPLFLN100x, OLYMPUS) was used in the optical microscope to identify individual microspheres and capture WGM emission data along with μ-PL imaging. Photoexcitation was achieved using a 470-nm pulsed-diode laser and a 532-nm laser under ambient conditions.

Numerical Simulation: The WGM resonance spectra and electromagnetic field profiles were simulated using a commercial finite-difference time-domain solver (Ansys Lumerical). The emissions from the CPDs were modeled as a dipole source positioned near the PS particle (n = 1.59), and the optical power was monitored using a transmission box enclosing the dipole.

Perfectly matched layers were set in the *x* and *y* directions. The unknown CD-coated layer thickness (t_{CD}) and refractive index (n_{CD}) were predetermined using Lumerical's built-in particle swarm optimization algorithm to maximize the cross-correlation between the experimental and simulated spectra, yielding $t_{CD} \sim 29$ nm and $n_{CD} \sim 1.55$.

Supporting Information

Supporting Information is available from the Wiley Online Library or from the author.

Acknowledgments

This work was financially supported by the JSPS-Kakenhi Research Grant (grant number 24K17589). BKB acknowledges The Japan Society for the Promotion of Science (**JSPS**) for the JSPS Postdoctoral Fellowship. The authors acknowledge the Namiki foundry at NIMS for XRD, FL, TEM, and optical characterizations.

Received: ((will be filled in by the editorial staff))
Revised: ((will be filled in by the editorial staff))
Published online: ((will be filled in by the editorial staff))

References

[1] a) P. Aldhous, *Nature* **2005**, *434* (7030), 132, https://doi.org/10.1038/434132a; b) M. Pecht, S. Tiku, *IEEE Spectrum* **2006**, *43* (5), 37, https://doi.org/10.1109/MSPEC.2006.1628506; c) J. Zhang, Y. Liu, C. Njel, S. Ronneberger, N. V. Tarakina, F. F. Loeffler, *Nature Nanotechnology* **2023**, *18* (9), 1027, https://doi.org/10.1038/s41565-023-01405-3.

[2] a) OECD, E. U. I. P. Office, *Trade in Counterfeit and Pirated Goods*, **2016**; b) H. Zhang, D. Hua, C. Huang, S. K. Samal, R. Xiong, F. Sauvage, K. Braeckmans, K. Remaut, S. C. De Smedt, *Advanced Materials* **2020**, *32* (11), 1905486, https://doi.org/https://doi.org/10.1002/adma.201905486.

[3] O. European Union Intellectual Property, *Economic impact of counterfeiting in the clothing, cosmetics, and toys sectors in the EU*, European Union Intellectual Property Office, **2023**.

[4] a) W. Ren, G. Lin, C. Clarke, J. Zhou, D. Jin, *Advanced Materials* **2020**, *32* (18), 1901430, https://doi.org/https://doi.org/10.1002/adma.201901430; b) X. Wang, H. Dai, B. Li, X. Xu, J. Zhang, D. Liu, Y. Liu, Z. Liu, *Advanced Optical Materials* **2024**, *12* (14), 2302831,

https://doi.org/https://doi.org/10.1002/adom.202302831; c) A. R. Anwar, M. Mur, M. Humar, *ACS Photonics* **2023**, *10* (5), 1202, https://doi.org/10.1021/acsphotonics.2c01611.

[5] a) B. K. Barman, D. Hernández-Pinilla, T. D. Dao, K. Deguchi, S. Ohki, K. Hashi, A. Goto, T. Miyazaki, K. K. Nanda, T. Nagao, *ACS Applied Materials & Interfaces* **2024**, *16* (17), 22312, https://doi.org/10.1021/acsami.3c18035; b) Y.-C. Chen, X. Fan, *Advanced Optical Materials* **2019**, *7* (17), 1900377, https://doi.org/https://doi.org/10.1002/adom.201900377; c) C. Lin, R. Jungmann, A. M. Leifer, C. Li, D. Levner, G. M. Church, W. M. Shih, P. Yin, *Nat Chem* **2012**, *4* (10), 832, https://doi.org/10.1038/nchem.1451; d) M. Schubert, L. Woolfson, I. R. M. Barnard, A. M. Dorward, B. Casement, A. Morton, G. B. Robertson, P. L. Appleton, G. B. Miles, C. S. Tucker, S. J. Pitt, M. C. Gather, *Nature Photonics* **2020**, *14* (7), 452, https://doi.org/10.1038/s41566-020-0631-z; e) N. Toropov, G. Cabello, M. P. Serrano, R. R. Gutha, M. Rafti, F. Vollmer, *Light: Science & Applications* **2021**, *10* (1), 42, https://doi.org/10.1038/s41377-021-00471-3.

[6] a) A. Capocefalo, E. Quintiero, C. Conti, N. Ghofraniha, I. Viola, *ACS Applied Materials & Interfaces* **2021**, *13* (43), 51485, https://doi.org/10.1021/acsami.1c14972; b) J. Feng, W. Wen, X. Wei, X. Jiang, M. Cao, X. Wang, X. Zhang, L. Jiang, Y. Wu, *Advanced Materials* **2019**, *31* (36), 1807880, https://doi.org/https://doi.org/10.1002/adma.201807880; c) A. H. Fikouras, M. Schubert, M. Karl, J. D. Kumar, S. J. Powis, A. Di Falco, M. C. Gather, *Nature Communications* **2018**, *9* (1), 4817, https://doi.org/10.1038/s41467-018-07248-0; d) C.-Y. Su, C.-F. Hou, Y.-T. Hsu, H.-Y. Lin, Y.-M. Liao, T.-Y. Lin, Y.-F. Chen, *ACS Applied Materials & Interfaces* **2020**, *12* (43), 49122, https://doi.org/10.1021/acsami.0c14875; e) S. Yang, Y. Wang, H. Sun, *Advanced Optical Materials* **2015**, *3* (9), 1136, https://doi.org/https://doi.org/10.1002/adom.201500232.

[7] a) X. Feng, R. Lin, S. Yang, Y. Xu, T. Zhang, S. Chen, Y. Ji, Z. Wang, S. Chen, C. Zhu, Z. Gao, Y. S. Zhao, *Angewandte Chemie International Edition* **2023**, *62* (46), e202310263, https://doi.org/https://doi.org/10.1002/anie.202310263; b) Z. Gao, C. Wei, Y. Yan, W. Zhang, H. Dong, J. Zhao, J. Yi, C. Zhang, Y. J. Li, Y. S. Zhao, *Advanced Materials* **2017**, *29* (30), 1701558, https://doi.org/https://doi.org/10.1002/adma.201701558; c) Y. Lv, X. Xiong, Y. Liu, J. Yao, Y. J. Li, Y. S. Zhao, *Nano Letters* **2019**, *19* (2), 1098, https://doi.org/10.1021/acs.nanolett.8b04402; d) D. Okada, T. Nakamura, D. Braam, T. D. Dao, S. Ishii, T. Nagao, A. Lorke, T. Nabeshima, Y. Yamamoto, *ACS Nano* **2016**, *10* (7), 7058, https://doi.org/10.1021/acsnano.6b03188.

[8] K. J. Vahala, *Nature* **2003**, *424* (6950), 839, https://doi.org/10.1038/nature01939.

[9] D. Venkatakrishnarao, M. A. Mohiddon, R. Chandrasekar, *Advanced Optical Materials* **2017**, *5* (2), 1600613, https://doi.org/https://doi.org/10.1002/adom.201600613.
[10] E. Marino, H. Bharti, J. Xu, C. R. Kagan, C. B. Murray, *Nano Letters* **2022**, *22* (12), 4765, https://doi.org/10.1021/acs.nanolett.2c01011.
[11] P. T. Snee, Y. Chan, D. G. Nocera, M. G. Bawendi, *Advanced Materials* **2005**, *17* (9), 1131, https://doi.org/https://doi.org/10.1002/adma.200401571.
[12] B. K. Barman, H. Yamada, K. Watanabe, K. Deguchi, S. Ohki, K. Hashi, A. Goto, T. Nagao, *Advanced Science* **2024**, *11* (30), 2400693, https://doi.org/https://doi.org/10.1002/advs.202400693.
[13] Y. Shang, J. Zhou, Y. Cai, F. Wang, A. Fernandez-Bravo, C. Yang, L. Jiang, D. Jin, *Nature Communications* **2020**, *11* (1), 6156, https://doi.org/10.1038/s41467-020-19797-4.
[14] a) S. Kushida, D. Braam, C. Pan, T. D. Dao, K. Tabata, K. Sugiyasu, M. Takeuchi, S. Ishii, T. Nagao, A. Lorke, Y. Yamamoto, *Macromolecules* **2015**, *48* (12), 3928, https://doi.org/10.1021/acs.macromol.5b00707; b) J. E. Cheeney, S. T. Hsieh, N. V. Myung, E. D. Haberer, *Nanoscale* **2020**, *12* (17), 9873, https://doi.org/10.1039/D0NR00147C; c) C. Kersuzan, S. Celaj, W. Daney de Marcillac, T. Pons, A. Maître, *ACS Photonics* **2024**, *11* (4), 1715, https://doi.org/10.1021/acsphotonics.4c00023.
[15] Y. Li, Y. T. H. Cu, D. Luo, *Nature Biotechnology* **2005**, *23* (7), 885, https://doi.org/10.1038/nbt1106.
[16] D. Richter, M. Marinčič, M. Humar, *Lab on a Chip* **2020**, *20* (4), 734, https://doi.org/10.1039/C9LC01034C.
[17] a) F. Hu, C. Zeng, R. Long, Y. Miao, L. Wei, Q. Xu, W. Min, *Nat Methods* **2018**, *15* (3), 194, https://doi.org/10.1038/nmeth.4578; b) L. Shi, M. Wei, Y. Miao, N. Qian, L. Shi, R. A. Singer, R. K. P. Benninger, W. Min, *Nat Biotechnol* **2022**, *40* (3), 364, https://doi.org/10.1038/s41587-021-01041-z; c) Y. Zhao, Z. Xie, H. Gu, L. Jin, X. Zhao, B. Wang, Z. Gu, *NPG Asia Materials* **2012**, *4* (9), e25, https://doi.org/10.1038/am.2012.46; d) T. C. Preston, J. P. Reid, *J. Opt. Soc. Am. B* **2013**, *30* (8), 2113, https://doi.org/10.1364/JOSAB.30.002113.
[18] a) D. Okada, Z.-H. Lin, J.-S. Huang, O. Oki, M. Morimoto, X. Liu, T. Minari, S. Ishii, T. Nagao, M. Irie, Y. Yamamoto, *Materials Horizons* **2020**, *7* (7), 1801, https://doi.org/10.1039/D0MH00566E; b) Y. Fan, C. Zhang, Z. Gao, W. Zhou, Y. Hou, Z. Zhou, J. Yao, Y. S. Zhao, *Advanced Materials* **2021**, *33* (42), 2102586, https://doi.org/https://doi.org/10.1002/adma.202102586; c) J. Ruan, D. Guo, K. Ge, Z. Xu, F. Liu, T. Zhai, *Nano Research* **2023**, *16* (7), 10100, https://doi.org/10.1007/s12274-023-5709-8.

[19] a) B. K. Barman, D. Hernández-Pinilla, O. Cretu, R. Ohta, K. Okano, T. Shiroya, J. Sasai, K. Kimoto, T. Nagao, *ACS Sustainable Chemistry & Engineering* **2023**, *11* (33), 12291, https://doi.org/10.1021/acssuschemeng.3c01775; b) B. K. Barman, K. Okano, K. Deguchi, S. Ohki, K. Hashi, A. Goto, T. Nagao, *ACS Sustainable Chemistry & Engineering* **2022**, *10* (49), 16125, https://doi.org/10.1021/acssuschemeng.2c04014; c) H. Kim, Y. Park, S. Beack, S. Han, D. Jung, H. J. Cha, W. Kwon, S. K. Hahn, *Advanced Science* **2017**, *4* (11), 1700325, https://doi.org/https://doi.org/10.1002/advs.201700325; d) X. Wen, P. Yu, Y.-R. Toh, X. Hao, J. Tang, *Advanced Optical Materials* **2013**, *1* (2), 173, https://doi.org/https://doi.org/10.1002/adom.201200046; e) J. Wang, F. Peng, Y. Lu, Y. Zhong, S. Wang, M. Xu, X. Ji, Y. Su, L. Liao, Y. He, *Advanced Optical Materials* **2015**, *3* (1), 103, https://doi.org/https://doi.org/10.1002/adom.201400307; f) B. Wang, J. Yu, L. Sui, S. Zhu, Z. Tang, B. Yang, S. Lu, *Advanced Science* **2021**, *8* (1), 2001453, https://doi.org/https://doi.org/10.1002/advs.202001453.

[20] a) K. Jiang, L. Zhang, J. Lu, C. Xu, C. Cai, H. Lin, *Angewandte Chemie International Edition* **2016**, *55* (25), 7231, https://doi.org/https://doi.org/10.1002/anie.201602445; b) D. Li, P. Jing, L. Sun, Y. An, X. Shan, X. Lu, D. Zhou, D. Han, D. Shen, Y. Zhai, S. Qu, R. Zbořil, A. L. Rogach, *Advanced Materials* **2018**, *30* (13), 1705913, https://doi.org/https://doi.org/10.1002/adma.201705913; c) H. Yang, Y. Liu, Z. Guo, B. Lei, J. Zhuang, X. Zhang, Z. Liu, C. Hu, *Nature Communications* **2019**, *10* (1), 1789, https://doi.org/10.1038/s41467-019-09830-6.

[21] O. Gallo, R. Manduchi, *IEEE Transactions on Pattern Analysis and Machine Intelligence* **2011**, *33* (9), 1834, https://doi.org/10.1109/TPAMI.2010.229.

[22] a) B. K. Barman, Ø. Sele Handegård, A. Hashimoto, T. Nagao, *ACS Sustainable Chemistry & Engineering* **2021**, *9* (29), 9879, https://doi.org/10.1021/acssuschemeng.1c02791; b) C. Xia, S. Zhu, T. Feng, M. Yang, B. Yang, *Advanced Science* **2019**, *6* (23), 1901316, https://doi.org/https://doi.org/10.1002/advs.201901316.

[23] a) J. Schwan, S. Ulrich, V. Batori, H. Ehrhardt, S. R. P. Silva, *Journal of Applied Physics* **1996**, *80* (1), 440, https://doi.org/10.1063/1.362745; b) Z. Zafar, Z. H. Ni, X. Wu, Z. X. Shi, H. Y. Nan, J. Bai, L. T. Sun, *Carbon* **2013**, *61*, 57, https://doi.org/https://doi.org/10.1016/j.carbon.2013.04.065.

[24] a) H. Ding, J.-S. Wei, N. Zhong, Q.-Y. Gao, H.-M. Xiong, *Langmuir* **2017**, *33* (44), 12635, https://doi.org/10.1021/acs.langmuir.7b02385; b) R. Sato, Y. Iso, T. Isobe, *Langmuir* **2019**, *35* (47), 15257, https://doi.org/10.1021/acs.langmuir.9b02739.

[25] a) B. K. Barman, K. K. Nanda, *Green Chemistry* **2016**, *18* (2), 427, https://doi.org/10.1039/C5GC01405K; b) K. Holá, M. Sudolská, S. Kalytchuk, D. Nachtigallová, A. L. Rogach, M. Otyepka, R. Zbořil, *ACS Nano* **2017**, *11* (12), 12402, https://doi.org/10.1021/acsnano.7b06399; c) J. M. Ripalda, E. Román, N. Díaz, L. Galán, I. Montero, G. Comelli, A. Baraldi, S. Lizzit, A. Goldoni, G. Paolucci, *Physical Review B* **1999**, *60* (6), R3705, https://doi.org/10.1103/PhysRevB.60.R3705.

[26] a) C. J. Reckmeier, J. Schneider, A. S. Susha, A. L. Rogach, *Opt. Express* **2016**, *24* (2), A312, https://doi.org/10.1364/OE.24.00A312; b) S. Zhu, Q. Meng, L. Wang, J. Zhang, Y. Song, H. Jin, K. Zhang, H. Sun, H. Wang, B. Yang, *Angewandte Chemie International Edition* **2013**, *52* (14), 3953, https://doi.org/https://doi.org/10.1002/anie.201300519.

[27] a) N. V. Tepliakov, E. V. Kundelev, P. D. Khavlyuk, Y. Xiong, M. Y. Leonov, W. Zhu, A. V. Baranov, A. V. Fedorov, A. L. Rogach, I. D. Rukhlenko, *ACS Nano* **2019**, *13* (9), 10737, https://doi.org/10.1021/acsnano.9b05444; b) F. Yan, Z. Sun, H. Zhang, X. Sun, Y. Jiang, Z. Bai, *Microchimica Acta* **2019**, *186* (8), 583, https://doi.org/10.1007/s00604-019-3688-y; c) S. Hu, A. Trinchi, P. Atkin, I. Cole, *Angewandte Chemie International Edition* **2015**, *54* (10), 2970, https://doi.org/https://doi.org/10.1002/anie.201411004.

[28] L. Wang, S.-J. Zhu, H.-Y. Wang, S.-N. Qu, Y.-L. Zhang, J.-H. Zhang, Q.-D. Chen, H.-L. Xu, W. Han, B. Yang, H.-B. Sun, *ACS Nano* **2014**, *8* (3), 2541, https://doi.org/10.1021/nn500368m.

[29] F. Vollmer, S. Arnold, *Nature Methods* **2008**, *5* (7), 591, https://doi.org/10.1038/nmeth.1221.

[30] A. N. Oraevsky, *QUANTUM ELECTRONICS* **2002**, *32* (5), 377, https://doi.org/10.1070/QE2002v032n05ABEH002205.

[31] a) V. B. Kumar, A. K. Sahu, A. S. M. Mohsin, X. Li, A. Gedanken, *ACS Applied Materials & Interfaces* **2017**, *9* (34), 28930, https://doi.org/10.1021/acsami.7b08985; b) Y. Ni, X. Li, W. Liang, S. Zhang, X. Xu, Z. Li, L. Li, Y. Shao, S. Ruan, W. Zhang, *Nanoscale* **2021**, *13* (16), 7566, https://doi.org/10.1039/D1NR00927C.

This study explores spectrally tunable photonics barcodes using carbonized polymer dots (CPDs) based on whispering gallery mode (WGM) photoluminescence. CPDs offer wavelength-dependent emission from visible to near-infrared (NIR), thereby enabling variable WGM emissions. These barcodes are easily decoded via excitation wavelength changes, providing a high encoding capacity without structural modifications ideal for applications in multiplexed assays, anti-counterfeiting, and product authentication.

B. K. Barman, K. Watanabe, T. Nagao

Carbonized Polymer Dots -based Spectrally Adaptable Photonic Microbarcodes